



HAL
open science

Site-specific hydrogen reactivity of $\text{Zn}_{0.05}\text{Mg}_{0.95}\text{O}$ nanopowders

Francia Haque, Fabio Finocchi, Stéphane Chenot, Jacques Jupille, Slavica Stankic

► **To cite this version:**

Francia Haque, Fabio Finocchi, Stéphane Chenot, Jacques Jupille, Slavica Stankic. Site-specific hydrogen reactivity of $\text{Zn}_{0.05}\text{Mg}_{0.95}\text{O}$ nanopowders. *Journal of Physical Chemistry C*, In press, 125 (46), pp.25841-25850. hal-03412053

HAL Id: hal-03412053

<https://hal.science/hal-03412053>

Submitted on 2 Nov 2021

HAL is a multi-disciplinary open access archive for the deposit and dissemination of scientific research documents, whether they are published or not. The documents may come from teaching and research institutions in France or abroad, or from public or private research centers.

L'archive ouverte pluridisciplinaire **HAL**, est destinée au dépôt et à la diffusion de documents scientifiques de niveau recherche, publiés ou non, émanant des établissements d'enseignement et de recherche français ou étrangers, des laboratoires publics ou privés.

Site-specific hydrogen reactivity of $\text{Zn}_{0.05}\text{Mg}_{0.95}\text{O}$ nanopowders

*Francia Haque, Fabio Finocchi, Stéphane Chenot, Jacques Jupille and Slavica Stankic**

Université, CNRS, Institut des NanoSciences de Paris, INSP, F-75005 Paris, France.

*E-mail: slavica.stankic@insp.jussieu.fr

KEYWORDS: Surface reactivity, $\text{Zn}_x\text{Mg}_{1-x}\text{O}$, nanopowders, DFT, hydrogen adsorption.

ABSTRACT

Here we present a combined theoretical and experimental study of hydrogen adsorption on Zn-functionalized MgO surface. We have systematically compared infrared spectra recorded at increasing hydrogen pressure (10^{-5} –100 mbar) on rock salt $\text{Zn}_{0.05}\text{Mg}_{0.95}\text{O}$ and MgO nanocubes. The interpretation of vibrations involving hydrogen was supported by *ab initio* calculations following the same strategy as for pure MgO. Despite the small Zn concentration, we unambiguously recorded Zn-specific signals. Most interestingly, we find that all chemisorption complexes characteristic of MgO surface reactivity remain highly preserved on $\text{Zn}_{0.05}\text{Mg}_{0.95}\text{O}$, while the effect of segregated Zn is strongly localized to its first oxygen neighbors. From the intensity variation of the IR couples when passing from spectra of pure to Zn-modified MgO, we (1) confirm the validity of the adsorption models that we previously proposed for MgO and (2) show that Zn segregates preferentially on low-coordination Mg surface sites (88% and 50%

substitution at corners and step edges, respectively). This study demonstrates that hydrogen can serve as a specific probe for low-coordinated Zn surface sites on $Zn_xMg_{1-x}O$ due to a higher H^- affinity of Zn^{2+} than Mg^{2+} cations.

1. Introduction

There is a general agreement on the fact that the surface functionalization of nanomaterials may promote novel physico-chemical properties.^{1,2} Decoration of graphene by transition metals or addition of dopants like boron and nitrogen significantly improve the poor hydrogen storage capabilities of pristine graphene.³ Substitution of Fe in the $V_2O_3(0001)$ surface increases the reducibility of the resulting mixed metal oxide surface.⁴ Enhanced corrosion resistance and biocompatibility of the Ti surfaces was attained by chemical modifications with ZnO thin films and organic bifunctional molecules.⁵ Surface modification of iron oxide makes them useful as nano-sorbents in purification of waste water.⁶ However, the protocol of substitution generally differs when passing from a material to another and the nature of the surface sites that are involved in the functionalization are seldom analyzed in detail and firmly identified. Actually, this step is crucial in view of designing nanomaterials with selected reactivity, bio-compatibility or with specific electronic and optical properties.⁷ MgO nanocrystals are here an archetype. MgO is widely used in surface science and catalysis since its most stable surface, namely MgO (001), is non-polar and does not undergo considerable structural relaxation.⁸ When synthesized in controlled conditions, MgO nanopowders reveal high thermal stability, nearly perfect cubic shape⁹ and can reach a specific surface area of $\sim 350 \text{ m}^2\text{g}^{-1}$.¹⁰

These characteristics – in particular the exceptionally large surface area – make such MgO nanocrystals a reliable model for surface functionalization and, hence, for the subsequent studies

on the correlation between doping and reactivity. Significant changes in surface reactivity (and thermal stability) were observed when only 0.2 % of Li^+ ions were admixed to MgO. In this study all IR fingerprints related to MgO were shown to become altered even though the maximum concentration of the active sites on the undoped MgO surface corresponds roughly to 3% of the total surface sites.¹¹ When doping MgO with Ca^{2+} an enhanced and red-shifted photoluminescence emission was achieved with respect to its parent oxides, CaO and MgO.¹² The study of the photonic behavior in $\text{Sr}_x\text{Mg}_{1-x}\text{O}$ nanopowders revealed a blue-shifted PL maximum compared to pure MgO¹³ that is, however, exactly opposite to that observed in $\text{Ca}_x\text{Mg}_{1-x}\text{O}$ nanopowders.¹² In this context, the most studied system is ZnO-MgO, which mixes a semiconductor and an insulator and whose band gap goes from 3.37 to 7.8. At the two ends of the phase diagram, Mg-doped ZnO and Zn-doped MgO keep the ZnO wurtzite and MgO cubic structure, respectively, while the medium composition range consist in a mixture of the two phases.¹⁴⁻¹⁶ In addition to the optical and semiconductor properties which are based in particular on the variable band gap¹⁴⁻¹⁶, $\text{Zn}_x\text{Mg}_{1-x}\text{O}$ combines the rich surface chemistry of the two parent oxides and has multiple catalytic¹⁷⁻¹⁹, photocatalytic^{20,21}, antibacterial²²⁻²⁴ and antifungal applications.²⁵ Changes in surface chemistry clearly correlate with dopant-induced electronic states that show up in valence bands of mixed oxides.^{17,26} However, little is known to which extent doping atoms perturb the matrix of the host oxide. In particular, a crucial issue is to know whether the doping modifies the sites only locally^{19,27} or if, conversely, it induces a charge redistribution which affects a wider neighborhood.

Adsorbed protons are of great relevance to probe MgO and ZnO surfaces. This is due to the extreme sensitivity of O-H and metal-H stretching frequencies towards changes in bond distances caused by charge transfers.^{28,29} This has motivated the present Fourier transform

infrared spectroscopy (FTIR) study of hydrogen adsorption on $\text{Zn}_{0.05}\text{Mg}_{0.95}\text{O}$ nanopowders. The choice of the Mg-rich side of the ZnO-MgO phase diagram was simply motivated by the cubic rock salt structure of Zn-doped MgO nanoparticles, which appears much more tractable than Mg-doped ZnO whose wurtzite structure is expected to involve a fairly complex set of facet orientations.³⁰ Moreover, for zinc concentrations lower than 10 at. %, only selective modifications of the edges in MgO cubes in form of $\text{Zn}^{2+}-\text{O}^{2-}$ scaffold-like structures were observed while the shape and cubic phase of pure MgO remain preserved.³¹ Indeed, the Mg^{2+} substitution by Zn^{2+} at the surface of MgO provides stabilization of the otherwise unstable cubic ZnO, which can be achieved only at high-pressures (2-9 GPa). By comparison with the heterolytic H_2 splitting on pure MgO nanocrystals, it is foreseen to point out the specific role of Zn^{2+} that replaces Mg^{2+} at the surface and show in which respects the reactivity of $\text{Zn}_x\text{Mg}_{1-x}\text{O}$ nanopowders differs from pure MgO nanopowders and why. First, we focus on the morphological characteristics and optical properties; then, we analyze the IR absorption spectra, which evolve as a function of the H_2 partial pressure (P_{H_2}). By comparison with DFT calculations of the hydrogen adsorption enthalpy on model surface sites at $\text{Zn}_x\text{Mg}_{1-x}\text{O}$ (001) surfaces, and the corresponding OH, H-Mg and H-Zn stretching frequencies, we propose an explanation for the monitored changes in terms of sites that show the highest reactivity towards H_2 .

2. Experimental and computational details

2.1 Synthesis, FTIR measurements and characterization techniques (DR UV-Vis, TEM)

Measurements have been performed in an UHV apparatus involving a preparation chamber and a main chamber – both including working pressure in the 10^{-10} mbar range. Fourier

Transform Infrared Spectroscopy (FTIR) was performed on MgO pellets in the main chamber (through ZnSe windows) in the transmission mode by means of a Bruker Vertex 70 FTIR spectrometer equipped with an MCT detector. Blanks were collected prior to exposure and used as references. $\text{Zn}_{0.5}\text{Mg}_{0.95}\text{O}$ powders were obtained via CVS technique.³¹ As starting material, high purity Zn and Mg pieces (> 99.98%) supplied by Goodfellow were used. The Zn^{2+} and Mg^{2+} concentrations were determined by atomic absorption spectroscopy (Analyst 100, Perkin-Elmer). The $\text{Zn}_{0.5}\text{Mg}_{0.95}\text{O}$ powder was pressed into pellets with the pressure applied less than 5 bar to avoid any changes in the specific surface area. Prior to being transferred in the main analysis chamber, $\text{Zn}_{0.5}\text{Mg}_{0.95}\text{O}$ pellets were degassed at 1170 K in UHV for one hour in the preparation chamber. The applied annealing treatment guarantees adsorbate-free $\text{Zn}_{0.5}\text{Mg}_{0.95}\text{O}$ surfaces, which was confirmed by absence of any adsorbed impurity in the initial infrared spectrum. Reference spectra used for the subtraction were recorded on the $\text{Zn}_{0.5}\text{Mg}_{0.95}\text{O}$ pellet degassed in UHV. Hydrogen that was used for the adsorption was supplied by Air Liquide with purity 99.999%. The IR spectra were recorded with a resolution of 4 cm^{-1} by averaging 250 interferogram scans to obtain a reasonable signal-to-noise ratio. For the purpose of subsequent transmission electron microscopy (TEM) and diffuse reflectance UV-vis (DR UV-Vis) spectroscopy measurements, the powders were also thermally activated at 1170 K in HV ($P < 10^{-6}$ mbar). In order to prevent any contact of the powder with the ambient air, the TEM grid was transported in a vacuum cell before microscopy measurements. However, while inserting it into the microscope, this could not be fully avoided in a time scale of around 5 minutes. The TEM analysis of the particles was achieved by using a JEOL 2100 field emission transmission electron microscope operated at 200 kV with a 0.18 nm resolution. The statistics used to plot each particle size distribution (PSD) involved the observation of more than 300 particles. The DR UV-vis

spectra were recorded at room temperature using a Varian Cary 5000 spectrometer equipped with an integrating sphere, while a sample of barium sulfate (BaSO_4) with $\sim 100\%$ reflectance was used as a reference. Spectra were collected in the presence of molecular oxygen ($P_{\text{O}_2}=10$ mbar) in order to quench the photoluminescence.

2.2 DFT calculations

The calculations have been carried out by using the DFT-based suite QuantumEspresso within the generalized gradient approximation (PBE)³² to density functional theory (DFT).³¹ We accounted for the interaction between the ionic cores and the valence electrons by ultra-soft pseudopotentials, with 40 Ry cutoff on the plane-wave expansion of the Kohn-Sham orbitals. The vibrational modes (frequencies and atomic displacements) were computed through the Density Functional Perturbation Theory (DFPT) in the harmonic approximation.³³ We carried out benchmark calculations on known molecules (MgH_2 , ZnH_2 and H_2O) to align the calculated frequencies on the measured ones. We used several slabs with periodic boundary conditions; they were at least 7 atomic (001) layers thick, up to 9 layers in the slabs with diatomic steps. The slabs were fully relaxed, apart from the fixed central layer. We inserted a void space between the periodic images of the slab that was 12 Å as thick. Within the previous choices, the adsorption energies and frequencies upon hydrogen adsorption were not biased by the slab thickness and the void space. In most cases, the unit cell was big enough to have a small Brillouin zone that can be accordingly sampled with the Gamma point. In order to obtain a clear comparison between the simulations of pure MgO and mixed $\text{Zn}_x\text{Mg}_{1-x}\text{O}$ nanopowders, we used most of the structural models that we employed in Ref. 29, by replacing the Mg cations at low-coordinated sites (3C or 4C) with Zn. We tested a few models differing by the site replacements and analyzed the structural details (bond lengths and angles). Then, we tested the adsorption of H_2 on several non-equivalent low-coordinated sites. As in pure MgO nanopowders, the hydrogen adsorption resulted to be dissociative on the low-coordinated O and Zn sites. Then, we computed the

corresponding adsorption energies, the bond lengths involving H^+ and H^- and the stretching frequencies.

3. Results

3.1. The $Zn_{0,05}Mg_{0,95}O$ nanocubes.

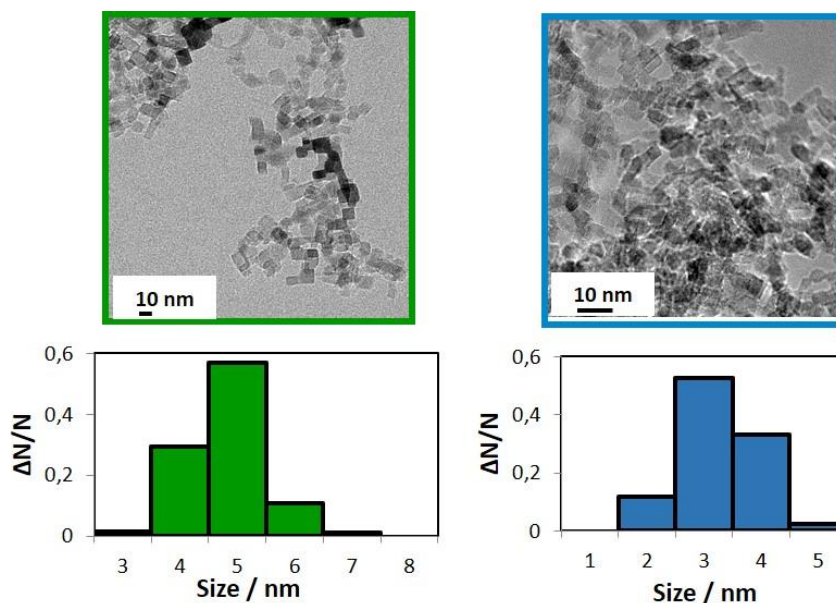


Figure 1: TEM images and size distribution diagrams of MgO (green) and $Zn_{0,05}Mg_{0,95}O$ (blue).

TEM images and particle size distributions of MgO and $Zn_{0,05}Mg_{0,95}O$ nanoparticles are shown in Figure 1. TEM images show that both powders consist of cubically shaped nanoparticles as usually found for pure MgO nanocrystals obtained by CVS.²⁹ As previously observed, the cubic shape specific of MgO pure nanocrystals is preserved in $Zn_xMg_{1-x}O$ nanopowders for $x < 0.15$.³¹ An important difference regards the size. While in the case of MgO the particles are ~ 5 nm wide on average – in line with that of the Ref. 29 – the mean size of $Zn_{0,05}Mg_{0,95}O$ nanocrystals is reduced to 3-3.5 nm. This smaller size is also reflected by a higher degree of the light scattering

as seen in the absorption spectrum between 350-500 nm (blue curve, Figure 2). The second parent oxide, namely CVS-ZnO, reveals nanoparticles that are much different in terms of both, the shape and size,³⁴ when compared to $\text{Zn}_{0.05}\text{Mg}_{0.95}\text{O}$ nano-oxide. Typical tetrapod-like ZnO structures of relatively large size can be seen in the inset of Figure 2. Relying on X-ray diffraction spectra (Figure S1), we exclude the phase separation and, thus, the presence of pure ZnO wurtzite in the mixed $\text{Zn}_{0.05}\text{Mg}_{0.95}\text{O}$ powder and we assume that the ternary oxide is entirely crystallized in the cubic structure. This is consistent with the phase diagram of the Zn-Mg-O system which, up to 40 at. % Zn, describes a solid solution of ZnO in MgO.³⁵ On the basis of the findings for the bulk Zn-Mg-O solid solutions and the ZnMgO nanopowders, Zn is expected to be incorporated in the MgO network in particular by replacing the Mg^{2+} cation at the surface.³¹ We firstly studied the effect of $\text{Mg}^{2+} \rightarrow \text{Zn}^{2+}$ substitution on the optical properties of MgO by means of UV absorption spectroscopy, as this technique is highly reliable for probing the atomistic structure of specific surface topological features.^{36,37} DR UV-Vis spectrum of $\text{Zn}_{0.05}\text{Mg}_{0.95}\text{O}$ nanopowder is compared in Figure 2 with the spectra of its two parent oxides (MgO and ZnO). In agreement with previous reports,^{36,37} the spectrum of MgO (Figure 2, green curve) consists of two distinct absorption bands at ~ 220 and ~ 270 nm that are respectively associated with the electronic transitions involving 4-fold (4C) and 3-fold (3C) coordinated surface elements. In the spectrum recorded on $\text{Zn}_{0.05}\text{Mg}_{0.95}\text{O}$, the spectral components are shifted to longer wavelengths and, in contrast to MgO, an absorption is observable even above 290 nm (below 4.3 eV). It is well documented that the incorporation of Zn^{2+} can lower the band gap of pure MgO via the Zn 4s states near the Fermi level.³⁸ This explains the additional absorption observed in $\text{Zn}_{0.05}\text{Mg}_{0.95}\text{O}$ spectrum, with the tendency towards lower energy especially after the absorption edge on pure CVS ZnO was observed at ~ 380 nm (Figure 2, black curve). Regarding

the absorption intensity, that is overall enhanced in $\text{Zn}_{0.05}\text{Mg}_{0.95}\text{O}$ spectrum, it can be to some extent related to an increased contribution of low coordinated surface sites of smaller $\text{Zn}_{0.05}\text{Mg}_{0.95}\text{O}$ particles (3 nm vs. 5 nm of pure MgO).⁴⁰ Both the red shift of the absorption maxima and the intensity increase of almost all MgO -specific absorption features appear to stem from the modification of MgO surface by zinc.

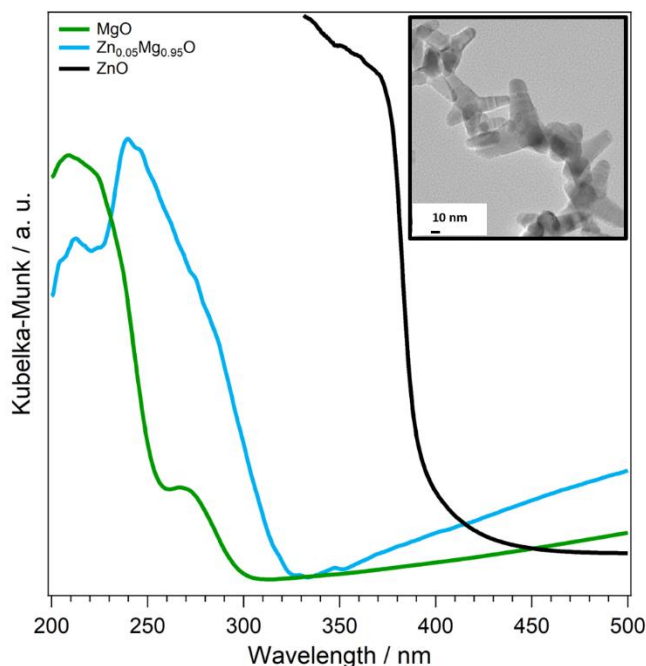


Figure 2: DR UV-Vis spectra of MgO (green) and $\text{Zn}_{0.05}\text{Mg}_{0.95}\text{O}$ (blue). The spectrum of pure ZnO (black) is added for the sake of comparison. The inset shows TEM image of pure CVS ZnO .

3.2. Hydrogen adsorption.

The effect of Zn^{2+} functionalization of the MgO surface was probed upon H_2 adsorption. We recorded FTIR spectra on $\text{Zn}_{0.05}\text{Mg}_{0.95}\text{O}$ nanopowders as a function of the partial hydrogen pressure P_{H_2} (Figure 3). As already pointed out for the case of pure MgO ,²⁹ a pressure higher

than 10^{-5} mbar is required to saturate the IR pellets by assuming a fast diffusion of hydrogen. Hence, the spectra recorded below this pressure are not quantitatively significant and we accordingly set the P_{H_2} range from 10^{-5} to 100 mbar. The evolution of spectra upon hydrogen adsorption is in many respects similar to what we observed on pure MgO nanocrystals.²⁹ Among the first detectable IR bands which appear up to $P_{H_2} = 10^{-3}$ mbar (hereafter labelled region A) are features that in pure MgO are attributed to the irreversible chemisorption complex I related to O_{3C} (3712 and 3699 cm^{-1}) and Mg inverse corners (Mg_{IC}) (1140, 930-970 and 863 cm^{-1}) – the latter being a site close to two interpenetrating (100) and (010) faces on MgO (001).²⁹ The intensities of all these features boost at $P_{H_2} > 10^{-3}$ mbar until they reach the saturation limit at $P_{H_2} \sim 1$ mbar (region B). At this hydrogen pressure, bands at 3610 cm^{-1} and 1225 cm^{-1} pop up in line with those seen on pure MgO upon H_2 adsorption and which were related to cooperative adsorption of stable and less stable bonding.²⁹ In parallel, bands specific to $Zn_{0.05}Mg_{0.95}O$ are recorded at 3745 cm^{-1} , 3610 cm^{-1} , 1780 cm^{-1} , 1680 cm^{-1} and 1510 cm^{-1} (see also Figure S2 for the three latter) since the very beginning of the exposure to hydrogen. Their intensity regularly increases up to $P_{H_2} = 100$ mbar. The high values of the hydride frequencies (1510-1780 cm^{-1}) indicate the involvement of Zn^{2+} ions, since the highest frequencies that we measured for MgH bands are at ~ 1400 cm^{-1} .²⁹ Finally, at $P_{H_2} \geq 1$ mbar (region C) FTIR reveals two prominent and sharp peaks at 3460 and 1325 cm^{-1} whose intensity promptly increases with the hydrogen pressure, as well as two bands of weak intensity at 1425 and ~ 1370 cm^{-1} . In pure MgO, this set of bands is referred to as reversible chemisorption complex II involving adsorption on O_{4C} and Mg_{3C} sites.²⁹ They are accompanied by IR features of more modest intensity at 3586 cm^{-1} , 1030 cm^{-1} and 890 cm^{-1} as well as by an additional increase of the shoulder at 3699 cm^{-1} (Figure 3) which were attributed to cooperative H_2 adsorption.²⁹

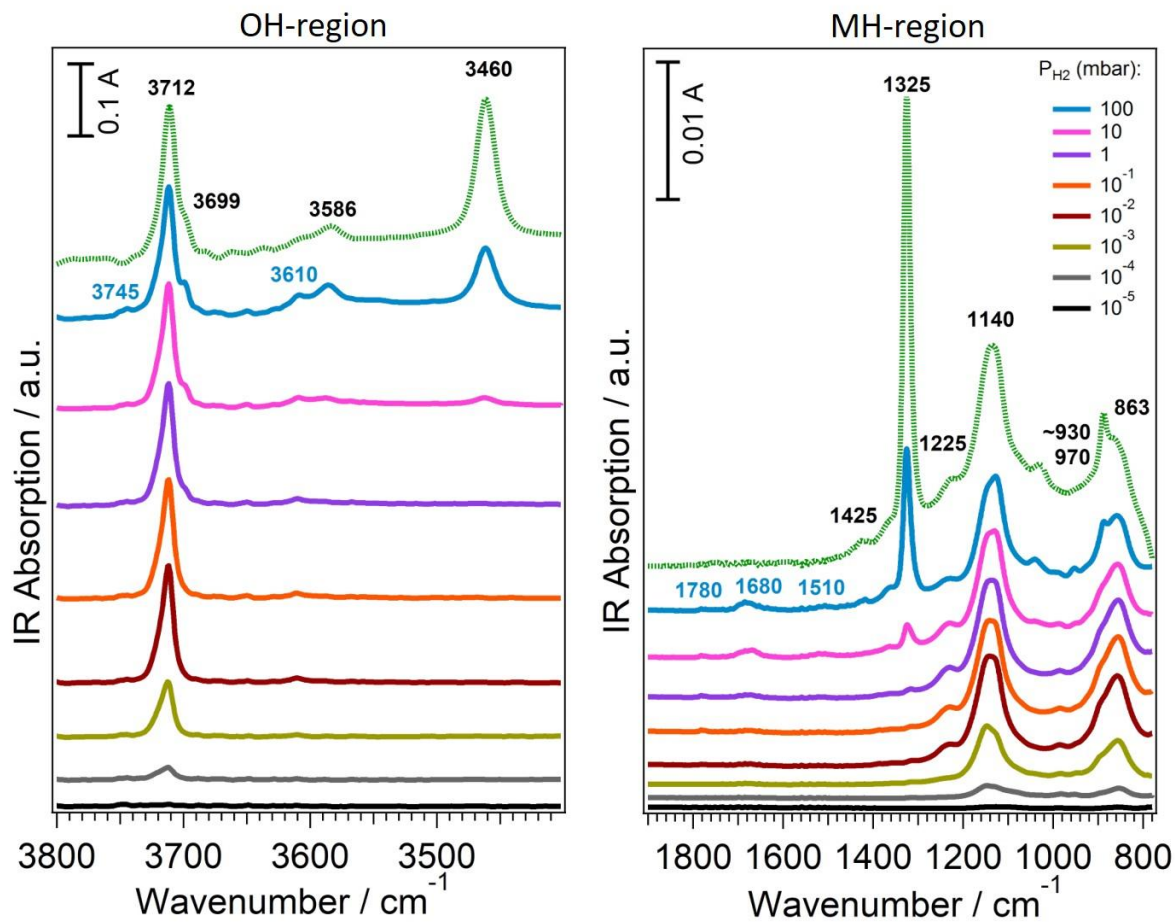


Figure 3: FTIR spectra of $\text{Zn}_{0.05}\text{Mg}_{0.95}\text{O}$ exposed to $P_{\text{H}_2} = 10^{-5} - 100$ mbar. The spectrum obtained on pure MgO at $P_{\text{H}_2} = 100$ mbar (dotted green) is added for the sake of comparison

Interestingly, the intensities of some bands observed at the highest P_{H_2} (100 mbar) show different trends in the two oxides. In the spectra of H/ZnMgO (Figure 3) the contributions associated to the chemisorption complex II (3460 and 1325 cm^{-1}) are of much smaller relative intensity with respect to those related to the chemisorption complex I (3712 and 1140 cm^{-1}) than in H/MgO

spectra (green curve, Figure 3). In other words, the inclusion of Zn seems to depress the reversible chemisorption complex II. To probe the stability of moieties formed by hydrogen adsorption on $\text{Zn}_{0.05}\text{Mg}_{0.95}\text{O}$ and MgO , FTIR spectra are recorded after H_2 desorption ($P_{\text{H}_2} = 10^{-8}$ mbar) and compared to those obtained at $P_{\text{H}_2} = 100$ mbar (Figure 4 a and b). Concerning the species formed below 10^{-3} mbar similar trends are observed in spectra of both oxides after H_2 removal. The intensities of the bands at 3712, 1140 and 863 cm^{-1} are little affected, in line with their attribution to the most stable surface configurations ($\text{O}_{3\text{C}}/\text{Mg}_{1\text{C}}$). As expected, the bands at 3605-3610 and 1225 cm^{-1} vanish since they are associated with the weak part of the cooperative adsorption responsible for the intensity increase of the Chemisorption complex I at P_{H_2} up to 1 mbar.²⁹ The bands at 3462, 1425, 1367 and 1325 cm^{-1} , that are related to the reversible chemisorption complex II (formed at $P_{\text{H}_2} > 1$ mbar) also disappear, except for faint residues at 1425 and around 1367 cm^{-1} particularly observable in case of $\text{Zn}_{0.05}\text{Mg}_{0.95}\text{O}$. Bands at 3586 and 880 cm^{-1} are cancelled. Conversely, the bands at 3699 cm^{-1} and the band at 1030 cm^{-1} – that appear in the same pressure range and are attributed to cooperative adsorption – are stable in vacuum.²⁹ In spectrum of $\text{Zn}_{0.05}\text{Mg}_{0.95}\text{O}$ (Figure 4a, grey curve), specific OH vibrations persist in the range $3640\text{-}3560\text{ cm}^{-1}$ along with the evolution of a new broad and unstructured band at $\nu < 3600\text{ cm}^{-1}$. The shoulder at 3745 cm^{-1} – detected only in H_2 -spectrum of $\text{Zn}_{0.05}\text{Mg}_{0.95}\text{O}$ (Figure 4a, blue curve) – reveals an intensity increase upon H_2 -desorption while the hydride bands ($1780\text{-}1510\text{ cm}^{-1}$) remain unchanged.

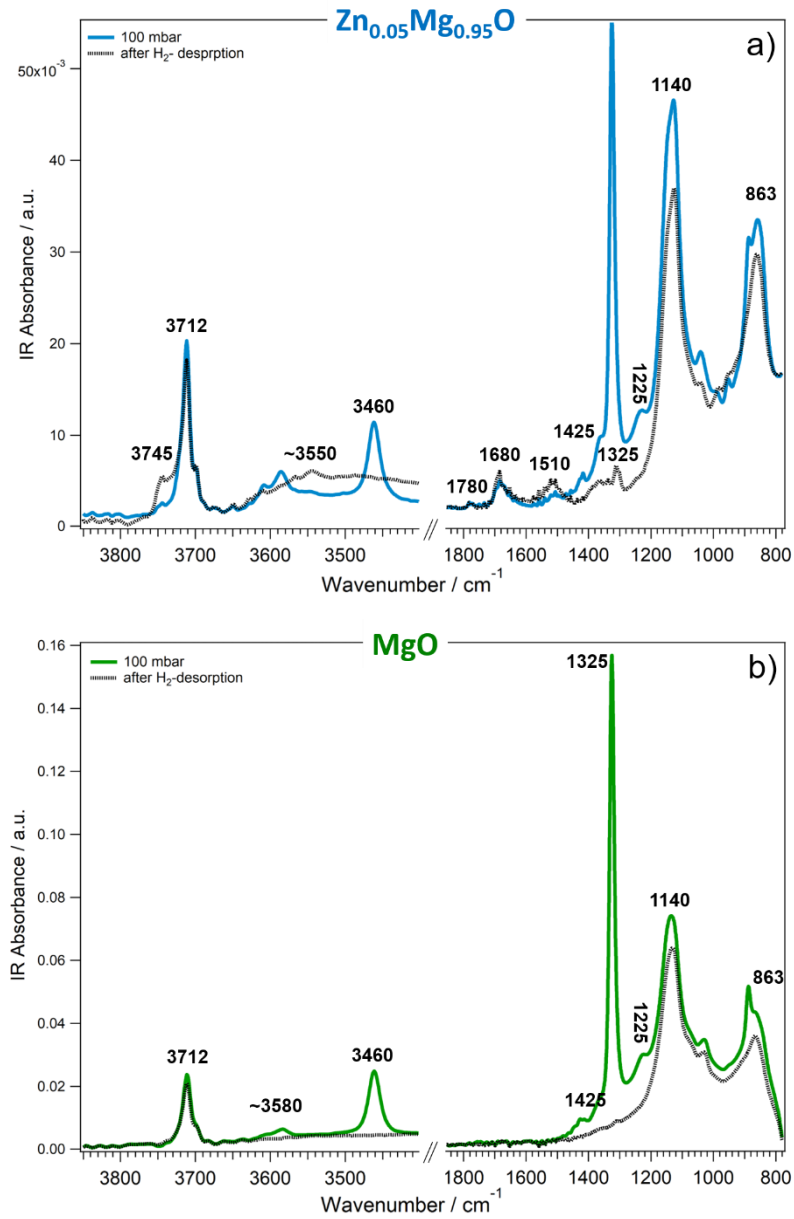


Figure 4: a) Comparison of the IR spectrum of $Zn_{0.05}Mg_{0.95}O$ exposed to $P_{H_2}=100$ mbar (blue curve) to that obtained at $P_{H_2}=10^{-8}$ mbar after hydrogen desorption (black curve). b) The same shown for MgO (spectra obtained at $P_{H_2}=100$ and after H_2 -desorption, green and black curves, respectively).

3.3. Simulations related to segregated Zn

The differences in UV-Vis spectra (Figure 2) and in H₂ adsorption (Figures 3 and 4) can be rationalized on the basis of the computed trends for the Mg²⁺ → Zn²⁺ substitution at MgO surface.³¹ At thermodynamic equilibrium, the replacement of Mg²⁺ by Zn²⁺ occurs preferentially at the under-coordinated surface defects following the sequence 3C → 4C → 5C sites, from the most to the less likely in the order. This is based on the segregation enthalpy which, among various surface configurations, is the most negative for the three-coordinated sites.³¹ In the same study we showed that the Zn²⁺ site occupancy can be computed for the ensembles of cubic particles as a function of particle temperature and size. Assuming perfect cubic shapes and a 3.5 nm average particle size as determined for Zn_{0.05}Mg_{0.95}O nanopowders, 88% of the total amount of Mg-3C sites (corners), ~ 50% of Mg-4C sites (step edges) and only 8% of Mg-5C sites are substituted by Zn on flat MgO (100) terraces. The replacement of bulk Mg²⁺ (6C) is below 1% and can be safely neglected. Such a substantial substitution of surface sites with the lowest coordination number changes therefore the chemical reactivity of the mixed nanopowders with respect to pure MgO ones.

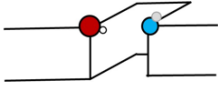
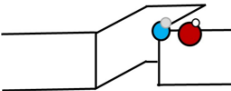

Before presenting the results of the simulations for H₂ on Zn_xMg_{1-x}O model surfaces, we remind the main trends that we found on pure MgO.²⁹ The principal computed adsorption characteristics (bond length, enthalpy, stretching frequencies) are strongly correlated to the site coordination number NC: for O_{NC}-H, the lower NC, the higher the adsorption enthalpy and the stronger (and shorter) the bond; conversely, anionic H⁻ prefers to bind to several Mg²⁺, in sites with low electrostatic (Madelung) potential. By combining the two trends, the two most stable complexes resulting from H₂ splitting are O_{3C}-H and H-Mg_{1C}. In sharp contrast, on Zn_xMg_{1-x}O nanocrystals, anionic H⁻ preferentially binds to low-coordinated Zn sites of which it is a specific probe, in a

similar way as cationic H^+ on O_{3C} . This inversion is ultimately due to the much higher hydrogen affinity for Zn than Mg. H_2 splitting is favored at Zn-O sites over Mg-O sites, whenever the former ones are available. H adsorption trends on $Zn_xMg_{1-x}O$ nanocrystals are therefore even simpler than on pure MgO: firstly, driven by coordination numbers, H_2 splitting preferentially occurs close to corners (3C) and step edges (4C) that are rich in Zn.

Simulations revealed that the three configurations shown in Table 1 were representative of all moieties formed by adsorption of H_2 on Zn atoms segregated at the surface of $Zn_xMg_{1-x}O$ nanocrystals. In any case, inverse corners on $Zn_xMg_{1-x}O$ nanocrystals are much less stable than split (H^- , H^+) at low-coordinated (3C, 4C) Zn-O sites. Computation also took in account the surface conformation (mono-atomic versus diatomic steps) and surrounding defect density (the presence or the absence of other Zn substituting Mg), which can bias the adsorption enthalpy, the bond lengths and thus the stretching frequencies only to a slight amount. Last but not least, as on pure MgO,²⁹ the formation of a weak electrostatic bond between cationic H^+ and anionic H^- that are adsorbed at neighboring sites stabilizes the O-H, H-Zn complexes and dilates the corresponding bonds, lowering the stretching frequencies by 1-2% at most. We found the same trend also in the case of hydrogen splitting on pure MgO nanocrystals.²⁹ For the configurations shown in Table 1, the rather high frequency computed at 3745 cm^{-1} corresponds to O_{3C} -H corners that are not first neighbors with Zn_{3C} . Those sites could be present on highly defective $Zn_xMg_{1-x}O$ nanocrystals, where steps, either mono- or poly-atomic, are likely not fully straight. Furthermore, we can see that the spectral signatures of the FTIR spectra around 1700 cm^{-1} and those around 1800 cm^{-1} come from Zn_{3C} . The computed H-Zn stretching frequencies in $Zn_xMg_{1-x}O$ found in the $1500\text{-}1895\text{ cm}^{-1}$ frequency range can unambiguously account for the FTIR bands experimentally observed at $1510\text{-}1780\text{ cm}^{-1}$. In particular, the H-Zn signal at 1680 cm^{-1} appears

at rather low hydrogen pressures and corresponds to anionic H^- adsorbed on Zn cations that replace Mg at corners (Table 1). We interpret those at lower frequencies, around 1500 cm^{-1} , as coming from H bound to Zn on step edges (Table 1).

Table 1. Calculated frequencies ($\tilde{\nu}$), bond lengths (d) and adsorption enthalpy (ΔH) for the most representative defect sites involving segregated Zn atoms (see text).

Type of defect	Model Complex	$\tilde{\nu}_{\text{OH}} (\text{cm}^{-1})$	$d_{\text{OH}}(\text{Å})$	$\tilde{\nu}_{\text{ZnH}} (\text{cm}^{-1})$	$d_{\text{ZnH}}(\text{Å})$	Adsorption enthalpy (eV/H ₂)
A: Monoatomic (and diatomic) step. H ⁺ , H ⁻ adsorption sites at O _{3C} , Zn _{3C}		3744 (3741)	0.971 (0.972)	1770 (1767)	1.556 (1.556)	-1.067 (-1.546)
B: Monoatomic (and diatomic) step. H ⁺ , H ⁻ adsorption sites at O _{4C} , Zn _{3C}		3654 (3695)	0.976 (0.974)	1854 (1895)	1.541 (1.528)	-1.169 (-1.113)
C: (510) surface with a double di-vacancy at the step. H ⁺ , H ⁻ adsorption sites at O _{4C} , Zn _{4C}		3630	0.977	1500	1.615	-0.759

● O²⁻ ● Mg²⁺ ● Zn²⁺ ● H⁺ ○ H⁻ Crystal

The computed adsorption enthalpy for a single H₂ molecule is in the (-1.1 -0.8) eV/H₂ range for 3C (corners) and 4C (step edge) sites. This is a lower value than what we found for most defects on pure MgO nanocrystals and corresponds to the formation of irreversible complexes (Table 1). The simulations indicate that inverse corners on Zn_xMg_{1-x}O nanocrystals are much less stable than (H⁻, H⁺) splitting at low-coordinated (3C, 4C) Zn-O sites (Supplementary Info of Ref.31). Therefore, H⁻ is a specific probe for low-coordinated Zn surface sites, which have a very high affinity for anionic hydrogen. H₂ splitting is favored at Zn-O sites over Mg-O sites, whenever the former ones are available.

Finally, as for H_2O^{41} and H_2 at $\text{MgO}(100)^{29}$, we find an inverse correlation between bond lengths and site coordination number. The computed OH bond lengths range between 0.971 and 0.975 Å for $\text{O}_{3\text{C}}$ sites (corners) and between 0.976 and 0.986, with a peculiarity at 0.994 Å for $\text{O}_{4\text{C}}\text{-H}$ at straight diatomic step edges. The Zn-H bond lengths range between 1.54 Å and 1.56 Å for $\text{Zn}_{3\text{C}}$ sites at corners, and between 1.56 and 1.61 Å for $\text{Zn}_{4\text{C}}$ sites at step edges. As a general trend, the lower the coordination number of the O^{2-} anion (Zn^{2+} cation) to which hydrogen binds, the shorter and stronger the bond is.^{42,43} The robust correlation between adsorption enthalpy, bond strength and stretching frequencies is confirmed in the case of ternary $\text{Zn}_x\text{Mg}_{1-x}\text{O}$ nanopowders, which thus make no exception to the general rule. Shown in Figure 5, the inverse linear regression between the O-H (H-Zn) bond lengths and the O-H (H-Zn) stretching frequencies is a guideline to identify, at the atomic scale, the surface configurations which are at the origin of the measured frequencies.

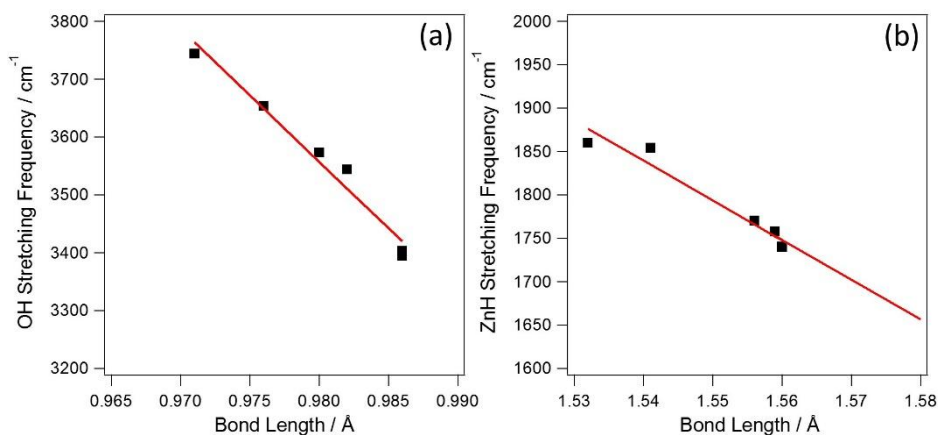


Figure 5: OH stretching frequencies on $\text{Zn}_x\text{Mg}_{1-x}\text{O}$: correlation between computed (a) $\text{O}^{2-}\text{-H}^+$ rescaled frequencies and $\text{O}^- \text{-H}^+$ bond lengths and (b) $\text{H}^- \text{-Zn}^{2+}$ frequencies and $\text{H}^- \text{-Zn}^{2+}$ bond lengths.

4. Discussion

The experimental spectra show that already at low Zn concentration (< 5. at %) the substitution of Mg^{2+} by Zn^{2+} results in significantly altered optical properties (Figure 2) and surface chemistry (Figure 3). In pure MgO the electronic transitions involve $\text{O}_{4\text{C}}$ and $\text{O}_{3\text{C}}$ surface sites that can be detected at 230 nm and 280 nm, respectively.^{36,40} In the DR UV-Vis spectrum of the $\text{Zn}_{0.05}\text{Mg}_{0.95}\text{O}$ powder (Figure 2), a red shift of all MgO specific absorption bands is observed along with an additional optical absorption at high energies ($\lambda > 290$ nm). Those trends are consistent with the optical absorption of pure ZnO which is red-shifted with respect to that of MgO. The fact that 88% of the total amount of Mg-3C sites (corners), ~ 50% of Mg-4C sites (step edges) and only 8% of Mg-5C sites are substituted by Zn (as shown in Section 3.3) leads to $\text{Zn}^{2+}\text{-O}^{2-}$ pairs that serve as an alternative channel for the optical excitations. The similarity and differences between $\text{Zn}_{0.05}\text{Mg}_{0.95}\text{O}$ and the pure MgO surfaces offer an opportunity to check the validity of the models that we employed to rationalize the hydrogen adsorption on both surfaces. Therefore, all observed vibrational frequencies involved in FTIR spectra recorded on $\text{Zn}_{0.05}\text{Mg}_{0.95}\text{O}$ upon P_{H_2} increase (Figure 3) are gathered in Table 2 together with the corresponding calculated configurations. In this Table from left to right the MgO-like sites are displayed in three regions A, B and C, defined as a function of the hydrogen pressure. ZnO sites are displayed in the right part of the Table 2. The corresponding frequencies are given for both, experimental (bold characters) and theoretical values (in brackets).

A principal observation is that the MgO-related frequencies previously observed on pure MgO nanoparticles are reproduced on $\text{Zn}_{0.05}\text{Mg}_{0.95}\text{O}$. These are dominated by three types of $\nu_{\text{OH}}/\nu_{\text{MgH}}$

pairs whose intensity and reversibility vary with P_{H_2} .²⁹ H_2 splitting at O corners ($\text{O}_{3\text{C}}$) and Mg inverse corners (Mg_{IC}) gives rise to the most stable complex (Chemisorption complex 1, presented in Table 2 in region A) that are accordingly populated at the lowest P_{H_2} applied (Region A, $P_{\text{H}_2} < 10^{-3}$ mbar). The corresponding stretching frequencies for $\text{O}_{3\text{C}}\text{H}$ are experimentally observed at 3712/3699 cm^{-1} and calculated at 3750/3740 cm^{-1} .²⁹ Regarding the $\text{Mg}_{\text{IC}}\text{-H}$, the experimental IR spectra consists in principle of three main bands²⁹: the two most dominant at 1140 and 850 cm^{-1} and a weak one observed between these two frequencies. Indeed, the five different models that were previously calculated to represent H-Mg_{IC} sites (Table 1 in Ref. 29) involve frequencies that systematically belong to two groups 1145-1095 cm^{-1} / 965-850 cm^{-1} whereas only one intermediate line predicted at 1020 cm^{-1} . This appears quite representative of the experiment in which the broad intense bands at 1140 and 850 cm^{-1} clearly result from several contributions. Then, the features of low intensity and of variable position which are observed between these two lines as a function of the pressure can be related to the calculated frequency of 1020 cm^{-1} . The intensity of the $\text{O}_{3\text{C}}/\text{Mg}_{\text{IC}}$ bands constantly grows with P_{H_2} along with the appearance of new bands at 3610/1225 cm^{-1} . The latter could be detected in the intermediate range of hydrogen pressures (Region B, $P_{\text{H}_2} = 10^{-3}$ –1 mbar) and stem from cooperative adsorption, which involves more than one H_2 ad-molecule at a time and allows for kinetically hindered, non-vicinal sites to be populated (presented in Table 2).²⁹ At high pressures ($P_{\text{H}_2} > 1$ mbar, region C) fully reversible adsorption occurs at neighboring $\text{O}_{4\text{C}}$ (either on mono- or diatomic steps) and $\text{Mg}_{3\text{C}}$ sites giving rise to the IR bands at 3460 and 1325 cm^{-1} , respectively (Chemisorption complex 2 presented in Table 2 in region C). In the same P_{H_2} range, we also observed an increase in intensity of the band at 3699 cm^{-1} and bands at 3586, 1030 and 888 cm^{-1} . These are attributed to a cooperative adsorption schematically represented by configuration D in

Table 1 of Ref. 29. In vacuum, the band associated to the reversible chemisorption complex II (3460 and 1325 cm^{-1}) vanish as well as those related to the weakly bonded moieties involved in cooperative adsorption (3610 and 1225 cm^{-1} , 3586 and 880 cm^{-1}).

The segregation of Zn at the MgO surface produces modifications of the hydrogen adsorption on the MgO sites which can be detected, as we will see, thanks to the preferential occupation of the low coordination Mg sites. It also leads to specific sites which we will consider next.

4.1. Preferential replacement of the low coordination Mg sites by Zn

Complex I and complex II require inverse corner sites (Mg_{IC}) and corner sites ($\text{Mg}_{3\text{C}}$). On $\text{Zn}_{0.05}\text{Mg}_{0.95}\text{O}$, the simulation predicts the replacement of 88% of $\text{Mg}_{3\text{C}}$ by Zn^{2+} , 50% of $\text{Mg}_{4\text{C}}$ and 8% of $\text{Mg}_{5\text{C}}$ by Zn^{2+} (Section 3.3). Thus, on $\text{Zn}_{0.05}\text{Mg}_{0.95}\text{O}$, the density of $\text{Mg}_{3\text{C}}$ and of Mg_{IC} is expected to reach 12% and 23% of what it is on pure MgO. This corresponds to a reduction by 50% of the bands related to the complex II ($\text{O}_{4\text{C}}\text{H}/\text{Mg}_{3\text{C}}\text{H}$, 3460/1325 cm^{-1}) with respect to those of complex I ($\text{O}_{3\text{C}}\text{H}/\text{Mg}_{\text{IC}}\text{H}$, bands at 3712/1140 cm^{-1} , Figure 3). However, the experimental reduction determined by band fitting is 70%. This value is meaningful since the area ratios observed for complex I and II on pure MgO ($\text{I}1140/\text{I}3712 = 7.54$ and $\text{I}1325/\text{I}3460 = 7.14$) and on $\text{Zn}_{0.05}\text{Mg}_{0.95}\text{O}$ ($\text{I}1140/\text{I}3712 = 7.40$ and $\text{I}1325/\text{I}3460 = 6.14$) only marginally differ. A suggestion to explain a reduction higher than expected might be a smaller segregation of Zn on sites close to inverse corners due to higher coordination number (more second neighbors) than on a common $\text{Mg}_{4\text{C}}$ edge site. Nevertheless, the observation qualitatively supports the theoretical prediction of a Zn replacement of the low-coordinated Mg sites on the ZnMgO surface.

Finally, the consistency of the hierarchy of the predicted decrease in density of the Mg sites (Mg_{3C} more decreased than Mg_{1C}) with the relative decrease of complex II with respect to complex I validates the models previously established for those complexes (Table 2).²⁹

4.2. H adsorption related to segregated Zn

As above mentioned, the main frequencies determined on $Zn_{0.05}Mg_{0.95}O$ upon H_2 exposure (3712, 3460, 1325, 1140 and 863 cm^{-1}) reproduce to within the unit of wave number those observed on pure MgO. As a result of Zn segregation, the second neighbors of hydrogen atoms involved in those configurations are statistically often Zn atoms. Therefore, we can retain as a guideline that the very local effect of segregated Zn is likely limited to its first oxygen neighbors.^{19,27}

The shoulder at 3745 cm^{-1} (Zn_{3C}/O_{3C} vs. Mg_{1C}/O_{3C})

An effect of non-uniform local Zn density may take place. This is for instance the case of the low-intensity signal at 3745 cm^{-1} which is observed only in the spectrum of $Zn_{0.05}Mg_{0.95}O$. This signal can be tracked in form of a shoulder (of the main peak at 3710 cm^{-1}) even at relatively low H_2 pressures, with intensity increasing steadily until the highest P_{H_2} of 100 mbar. As its intensity is always quite small compared to the main peak, the corresponding configurations should be marginal and occur quite seldom in $Zn_{0.05}Mg_{0.95}O$. The OH frequencies of the calculated surface structures with $O_{3C}H/Zn_{3C}H$ at mono- and di-atomic steps (Table 1, configuration A) are consistent with the experimentally observed values at 3745 cm^{-1} . The proposed structures contain, moreover, the Zn_{3C} sites, shown above to take the major contribution over Mg_{3C} in

$\text{Zn}_{0.05}\text{Mg}_{0.95}\text{O}$ powder. Their corresponding Zn-H frequencies, that were calculated at $\sim 1770\text{ cm}^{-1}$, will be discussed below. As for the 3745 cm^{-1} signal another interpretation, however, could imply atomic structures in which the oxygen corner ($\text{O}_{3\text{C}}$) is located in a Zn-rich environment, with quite a large proportion of $\text{Zn}_{4\text{C}}$ first-neighbors. Indeed, O-Zn bonds are slightly longer than O-Mg and whenever two or three Zn atoms are coordinated to this $\text{O}_{3\text{C}}$ (instead of three Mg-atoms) the $\text{O}_{3\text{C}}\text{-H}$ bond is slightly shorter. Consequently, the frequencies of such $\text{O}_{3\text{C}}\text{-H}$ must be higher (3745 cm^{-1}) than $\text{O}_{3\text{C}}\text{H}$ in pure MgO (3712 cm^{-1}). Interestingly, we observed similar OH stretching frequencies also in the IR spectrum of ZnO nanopowder (recorded upon water adsorption, see Figure S3) that we synthesized via the very same technique as used in the present work. Oxygen atoms located in a Zn-rich environment, such as in pure ZnO, result in higher OH-stretching frequencies than those observed on pure MgO nanoparticles upon water adsorption ($3711 - 3727\text{ cm}^{-1}$).⁴¹ Overall, the number of the corresponding configurations is likely quite small and, hence, results in a low IR intensity.

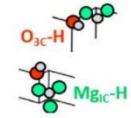
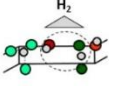
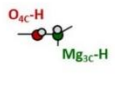
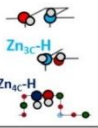
Finally, the desorption of H_2 from the $\text{Zn}_{0.05}\text{Mg}_{0.95}\text{O}$ surface reveals features that were not observed at the surface of pure MgO (Figure 4). The chemisorption complex II is not fully reversibly (1325 cm^{-1}) and there is also a broad feature around 3550 cm^{-1} . Moreover, an intensity enhancement of the band at 3745 cm^{-1} is observable. As obvious, at the $\text{Zn}_{0.05}\text{Mg}_{0.95}\text{O}$ surface there is likely a kind of Zn-induced surface reorganization upon H_2 adsorption/ desorption cycles.

New bands in the ZnH range (1780-1510 cm^{-1})

Three main ZnH bands can be distinguished in the experimental spectrum of $\text{Zn}_{0.05}\text{Mg}_{0.95}\text{O}$: $\sim 1780\text{ cm}^{-1}$, $\sim 1680\text{ cm}^{-1}$ and $\sim 1510\text{ cm}^{-1}$ (Figure S2). We recall that the intensity is proportional

to the dynamic dipole that is larger in Mg-H than in Zn-H. Therefore, the intensity of a single Zn-H stretching mode remains lower than that of its Mg-H counterpart. Relying on the DFT, Zn-H frequencies calculated for the structures that include O_{4C}/Zn_{3C} pairs (B, Table 1) are around $\sim 1850\text{ cm}^{-1}$ and fairly account for the experimentally observed ones in the highest frequency part of the Zn-H range ($\sim 1780\text{ cm}^{-1}$). Furthermore, the configuration A (Table 1) may explain the second series of Zn-H bands experimentally seen at $\sim 1680\text{ cm}^{-1}$. Finally, $Zn_{4C}H$ in structure C was calculated to vibrate at 1500 cm^{-1} , that is in a perfect match with the lowest Zn-H frequency experimentally observed ($\sim 1510\text{ cm}^{-1}$). The OH-counterpart of the structure C, that was not discussed above, yields $\nu_{OH} = 3630\text{ cm}^{-1}$ and can be representative of the experimentally observed value at $\sim 3610\text{ cm}^{-1}$. Despite slightly stronger intensity than in pure MgO, this experimental band is not clearly observable but rather masked by other frequencies in this region – previously shown to be specific of hybrid structures contributing in cooperative adsorption in pure MgO ($\sim 3600\text{ cm}^{-1}$). The same is true for the OH counterpart of the structure B (ν_{O_4CH} , Table 1) calculated at 3654 and 3695 cm^{-1} for the mono- and diatomic steps, respectively. In the experimental spectrum of $Zn_{0.05}Mg_{0.95}O$, the frequencies at these OH values are not observable as clearly isolated and new IR bands. We assume that they instead rather appear in form of parts of the already existing MgO-specific bands: the one at 3610 cm^{-1} (assigned in MgO to $O_{4C}H$ of hybrid structures) and the one at 3700 cm^{-1} ($O_{3C}H$ of the Chemisorption complex I in MgO).

Table 2. Assignment of FTIR frequencies observed in Figure 3: from left to right, the MgO-like sites displayed within three columns corresponding to regions A, B and C and the ZnO sites on the left. Stretching O-H and metal-H frequencies, presented in bold characters from high to low, are associated to their sites, O_{3C} (light red), O_{4C} (dark red), Zn_{3C} (light blue), Zn_{4C} (dark blue), Mg_{3C} and Mg-H-Mg (dark green) and Mg_{1C} (light green). Theoretical values are shown in brackets. Main schematic representations of the sites are shown at the bottom (Chemisorption complex I in region A, cooperative adsorption in region B in which the release of weakly adsorbed hydrogen is featured, Chemisorption complex II in region C and ZnO structures).

IR frequencies (cm ⁻¹): H ₂ adsorption on Zn _{0.05} Mg _{0.95} O surface			
MgO-like sites			ZnO sites
Region A: Irreversible complex I	Region B: Cooperative adsorption	Region C: Reversible complex II + Coop. ads.	Adsorption on segregated Zn
≥ 10 ⁻⁵ mbar	≥ 10 ⁻³ mbar	1-100 mbar	10 ⁻⁵ - 10 ⁻³ mbar
O_{3C}-H			3745 (3744)
3712 (3740-3750)	→ strengthens		
3699 (3710)		3699 strengthens	
O_{4C}-H			3610 (3630-3654)
	3605 (3545)		
		3586	
		3460 (3480-3508) Compl. II weakens /pure MgO	
Zn_{3C}-H			1680-1780 (1770-1854)
Zn_{4C}-H			1510 (1500)
Mg_{3C}-H		1325 (1390-1410) Compl. II weakens /pure MgO	
Mg_{4C}-H Mg_{5C}-H	1225 (1230)		
Mg_{1C}-H	1140 (1095-1145)	→ strengthens	
			1030 (1095-1105)
	950-980 (1020)		
			888
860 (850-965)	→ strengthens		
			
● Mg ● Zn ● O ○ H			

5. Conclusion

The adsorption of hydrogen at increasing pressure (10^{-5} to 100 mbar) on $\text{Zn}_{0.05}\text{Mg}_{0.95}\text{O}$ nanopowders has been studied by FTIR with the support of *ab initio* calculations. The ternary oxide keeps the cubic rock salt structure in which some Mg cations are substituted by Zn.

Despite the low Zn content of the compound, Zn is shown to segregate preferentially at low-coordinated surface sites (88% of the $\text{Mg}_{3\text{C}}$ corners and 50% of the $\text{Mg}_{4\text{C}}$ step edge cations are replaced by $\text{Zn}_{3\text{C}}$ and $\text{Zn}_{4\text{C}}$, respectively) and:

- The dissociative adsorption of hydrogen give rise to the same chemisorption complexes I (irreversible) and II (reversible) as on pure MgO nanopowders, as well as to similar cooperative adsorptions (which are, indeed, responsible for the intensity boost of the irreversible adsorption).
- The configurations that were previously modeled on pure MgO for complex I and II are confirmed by the analysis of the changes in relative intensity of the bands related to those complexes.

New bands are associated to Zn surface atoms. Their frequencies are fairly modeled by DFT.

Specific of pure MgO, the Mg-H and H-O stretching frequencies were reproduced on $\text{Zn}_{0.05}\text{Mg}_{0.95}\text{O}$ within the unit of wave number, the effect of segregated Zn is very localized to its first oxygen neighbors. This study shows that the MgO specific surface reactivity remains highly preserved in $\text{Zn}_{0.05}\text{Mg}_{0.95}\text{O}$ nanopowder despite the substantial substitution of Mg-surface sites by Zn.

ASSOCIATED CONTENT

Supporting Information

XRD spectra of MgO, Zn_{0.05}Mg_{0.95}O, and ZnO; FTIR spectra of Zn_{0.05}Mg_{0.95}O at P_{H2} = 10⁻⁵ – 100 mbar; FTIR spectra of CVS-ZnO at P_{H2O} = 10⁻⁸ – 10 mbar.

AUTHOR INFORMATION

Corresponding Author

*E-Mail: slavica.stankic@insp.jussieu.fr.

Funding Sources

No additional funding was provided.

ACKNOWLEDGMENT

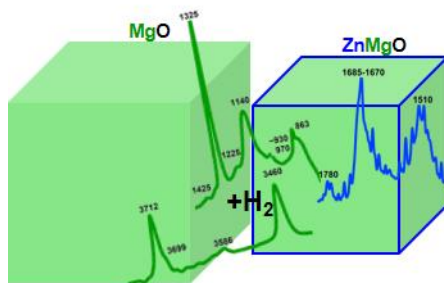
F. H. thanks l'Ecole Doctorale 397 for a doctoral research contract.

REFERENCES

- (1) Pebley A. C.; Decolvenaere E.; Pollock T. M.; Gordon M. J. Oxygen evolution on Fe-doped NiO electrocatalysts deposited via microplasma. *Nanoscale* **2017**, *9*, 15070-15082.
- (2) Livraghi S.; Paganini M.C.; Giamello E.; Di Liberto G.; Tosoni S.; Pacchioni GF. Formation of reversible adducts by adsorption of oxygen on Ce–ZrO₂: An unusual η² ionic superoxide. *J. Phys. Chem. C* **2019**, *123*, 27088-27096.
- (3) Jain, V.; Kandasubramanian, B. Functionalized graphene materials for hydrogen storage. *J Mater Sci.* **2020**, *55*, 1865–1903.
- (4) Jonayat A. S. M.; Kramer A.; Bignardi L.; Lacovig P.; Lizzit S.; van Duin A.C.T.; Batzill M.; Janik M.J. A first-principles study of stability of surface confined mixed metal oxides with corundum structure (Fe₂O₃, Cr₂O₃, V₂O₃) *Phys. Chem. Chem.* **2018**, *20*, 7073-7081.
- (5) Trino L.D.; Dias L.F.G.; Albano L.G.S.; Bronze-Uhle E.S.; Rangel E.C.; Graeff C.F.O.; Lisboa-Filho P.N. Zinc oxide surface functionalization and related effects on corrosion resistance of titanium implants. *Ceram. Int.* **2018**, *44*, 4000-4008.

- (6) Jinyue Yang J.; Hou B.; Wang J.; Tian B.; Bi J.; Wang N.; Li X.; Huang X. Nanomaterials for the Removal of Heavy Metals from Wastewater. *Nanomaterials* **2019**, *9*, 1-39.
- (7) Sternig A.; Diwald O.; Gross S.; Sushko P.V. Surface Decoration of MgO Nanocubes with Sulfur Oxides: Experiment and Theory. *J. Phys. Chem. C*, **2013**, *117*, 7727-7735.
- (8) Freund H.-J.; Heyde M.; Kühlenbeck H.; Nilius N.; Risse T.; Schmidt T.; Shaikhutdinov S.; Sterrer M. Chapter model systems in heterogeneous catalysis at the atomic level: a personal view. *Sci. Ch. Chem.* **2020**, *63*, 426–447.
- (9) Hacquart, R.; Krafft J.M.; Costentin G.; Jupille J. Evidence for emission and transfer of energy from excited edge sites of MgO smokes by photoluminescence experiments. *Surf. Sci.* **2005**, *595*, 172-182.
- (10) Hofmann, P.; Knözinger, E.; Diwald, O.; Mustafa: A. Thermally stable CaO surfaces on highly dispersed MgO — New aspects for methane activation. *Ber. Bunsenges. Phys. Chem.* **1997**, *101*, 1722-1727.
- (11) Berger T.; Schuh, J.; Sterrer, M.; Diwald O.; Knözinger E. Lithium ion induced surface reactivity changes on MgO nanoparticles. *J. of Catal.* **2007**, *247*, 61 – 67.
- (12) Stankic S.; Sterrer M.; Hofmann P.; Bernardi J.; Diwald O.; Knözinger E. Novel optical properties of Ca⁽²⁺⁾-doped MgO nanocrystals. *Nano Lett.* **2005**, *5*, 1889-1893.
- (13) Stankic S.; Bernardi J.; Diwald O.; Knözinger E. Photoexcitation of local surface structures on Strontium oxide grains. *J. Phys. Chem. C*, **2007**, *111*, 8069- 8074.
- (14) Choopun S.; Vispute R.D.; Yang W.; Sharma R.P.; Venkatesan T. Realization of band gap above 5.0 eV in metastable cubic-phase Mg_xZn_{1-x}O alloy films. *Appl. Phys. Lett.* **2002**, *80*, 1529–1531.
- (15) Takeuchi I.; Yang W.; Chang K.-S.; Aronova M. A.; Venkatesan T. Monolithic multichannel ultraviolet detector arrays and continuous phase evolution in Mg_xZn_{1-x}O composition spreads. *J. Appl. Phys.* **2003**, *94*, 7336-7440.
- (16) Lu G.; Lieberwirth I.; Wegne G. A general polymer-based process to prepare mixed metal oxides: The case of Zn_{1-x}Mg_xO Nanoparticles. *J. Am. Chem. Soc.* **2006**, *128*, 15445-15450.
- (17) Rodriguez J. A.; Pérez M.; Jirsak T.; Gonzalez L.; Maiti A.; Larese J. Z. DeNO_x Reactions on MgO (100), Zn_xMg_{1-x}O (100), Cr_xMg_{1-x}O (100), and Cr₂O₃(0001): Correlation between electronic and chemical properties of mixed-metal oxides. *J. Phys. Chem. B*, **2001**, *105*, 5497-5505.
- (18) Lee H.V.; Taufiq-Yap Y.H.; Hussein M.Z.; Yunus R. Transesterification of jatropha oil with methanol over Mg-Zn mixed metal oxide catalysts. *Energy* **2013**, *49*, 12-18.
- (19) Fonseca C.G.; Silva B.N.N.; Haddad J.F.S.H.; Lima L.L.; Moraes P.I.R.; Vaiss V.S.; Antunes F.P.N.; Souza W.F.; Chiaro S.S.X.; Leitão A.A. DFT simulations of dissociative chemisorption of sulfur-, nitrogen- and oxygen-containing molecules on mixed oxides with Mg, Al and Zn. *App. Surf. Sci.* **2019**, *484*, 524–533.
- (20) Etacheri V.; Roshan R.; Kuma V. Mg-Doped ZnO Nanoparticles for Efficient Sunlight-Driven Photocatalysis. *Appl. Mater. Interfaces* **2012**, *4*, 2717–2725.
- (21) Lian J.; Zhang C.; Li Q.; Ng D.H.L. Mesoporous (ZnO)_x(MgO)_{1-x} nanoplates: template-free solvothermal synthesis, optical properties, and their applications in water treatment. *Nanoscale* **2013**, *5*, 11672-11678.
- (22) Stankic S.; Suman S.; Haque F.; Vidic J. Pure and multi metal oxide nanoparticles: synthesis, antibacterial and cytotoxic properties, *J. of Nanobiotechn.* **2016**, *14*, 73.
- (23) Vidic J.; Stankic S.; Haque F.; Ciric D.; Le Goffic R.; Vidy A.; Jupille J.; Delmas B. Selective antibacterial effects of mixed ZnMgO nanoparticles. *J Nanopart. Res.* **2013**, *15*, 1595.
- (24) Rao Y.; Wang W.; Tan F.; Cai Y.; Lu Y.; Qiao X. Influence of different ions doping on the antibacterial properties of MgO nanopowders. *App. Surf. Sci.* **2013**, *284*, 726– 731.
- (25) Sierra-Fernandez A.; De la Rosa-García S. C.; Gomez-Villalba L. S.; Gómez-Cornelio S.; Rabanal M. E.; Fort R.; Quintana P. Synthesis, photocatalytic, and antifungal properties of MgO, ZnO and

- Zn/Mg Oxide nanoparticles for the protection of calcareous. *Appl. Mater. Interfaces* **2017**, *9*, 24873–24886.
- (26) Stavale F.; Nilius N.; Freund H.-J. STM luminescence spectroscopy of intrinsic defects in ZnO(000 $\bar{1}$) thin films. *J. Phys. Chem. Lett.* **2013**, *4*, 3972-3976.
- (27) Fonseca C.G.; Tavaresa S.R.; Soares C.V.; daFonseca B.G.; Henrique F.J.F.S. Vaiss V.S.; Souza W.F.; Chiaro S.S.X.; Diniz R.; Leitão A.A. The role of Zn²⁺ dopants in the acid-basic catalysis on MgO (001) surface: Ab initio simulations of the dissociative chemisorption of R-O-R' and R-S-R' (R, R' = H, CH₃, C₂H₅). *Surf. Sci.* **2017**, *661*, 60–68.
- (28) Finocchi F.; Hacquart R.; Naud C.; Jupille J. Hydroxyl-defect complexes on hydrated MgO smokes. *J. Phys. Chem. C* **2008**, *112*, 13226-13231.
- (29) Haque F.; Finocchi F.; Chenot S.; Jupille J.; Stankic S. Interplay between single and cooperative H₂ adsorption in the saturation of defect sites at MgO nanocubes. *J. Phys. Chem. C* **2018**, *122*, 17738 – 17747.
- (30) Haque F.; Chenot S.; Vines, F. Illas, Stankic S. and Jupille J. ZnO powders as multi-facet single crystals. *Phys. Chem. Chem. Phys.* **2017**, *19*, 10622 – 10628.
- (31) Stankic S.; Sternig A.; Finocchi F.; Bernardi J.; Diwald O. Zinc oxide scaffolds on MgO nanocubes. *Nanotechnology* **2010**, *21*, 355603.
- (32) Cavalleri, M.; Pelmeshnikov, A.; Morosi, G.; Gamba, A.; Coluccia, S.; Martra, G. M. Dissociative Adsorption of H₂ on Defect Sites of MgO: A Combined IR Spectroscopic and Quantum Chemical Study. *Studies in Surface Sci Catal.* **2001**, *140*, 131-139.
- (33) Shluger, A. L.; Gale, J. D.; Catlow, C. R. A. Molecular Properties of the Magnesia Surface. *J. Phys. Chem.* **1992**, *96*, 10389-10397.
- (34) Zhang M.; Averseng F.; Krafft J.-M.; Borghetti P.; Costentin G.; Stankic S. Controlled formation of native defects in ultrapure ZnO for the assignment of green emissions to oxygen vacancies. *J. Phys. Chem. C* **2020**, *124*, 12696–12704.
- (35) Segnit E. R.; Holland A. E. System MgO–ZnO–SiO₂. *J. Am. Ceram. Soc.* **1965**, *48*, 410–413.
- (36) Müller M.; Stankic S.; Diwald O.; Knözinger E.; Sushko P.; Trevisanutto P.; Shluger A. Effect of protons on the optical properties of oxide nanostructures *J. Am. Chem. Soc.* **2007**, *129*, 12491–12496.
- (37) Sternig A.; Stankic S.; Müller M.; Bernardi J.; Knözinger E.; Diwald O. Photoluminescent nanoparticle surfaces: the potential of alkaline earth oxides for optical applications. *Adv. Mater.* **2008**, *20*, 4840-4844.
- (38) Wang, J.; Tu, Y.; Yang, L.; Tolner, H. Theoretical investigation of the electronic structure and optical properties of zinc-doped magnesium oxide. *J. Comput. Electron* **2016**, *15*, 1521-1530.
- (39) Wobbe M. C. C.; Kerridge A.; Zwiijnenburg M. A. Optical excitation of MgO nanoparticles; a computational perspective. *Phys. Chem. Chem. Phys.* **2014**, *16*, 22052-22061.
- (40) Stankic S.; Müller M.; Diwald O.; Sterrer M.; Knözinger E.; Bernardi J. Size-dependent optical properties of MgO nanocubes. *Angew. Chem. Intern. Ed.* **2005**, *44*, 4917-4920.
- (41) Finocchi F.; Haque F.; Chenot S.; Jupille J.; Stankic S. Water dissociation on the low-coordinated sites of MgO nanopowders. *J. Mater. Res.* **2019**, 1-8.
- (42) Ferraris G.; Catti M. Generalization of Baur's correlations between bond length and bond strength in inorganic structures. *Acta Cryst. B* **1973**, *29*, 2006-2009.
- (43) Finocchi F.; Noguera C. Structure and bonding of small stoichiometric lithium oxide clusters. *Phys. Rev. B* **1996**, *53*, 4989.



TOC Image